Description of the mass-asymmetric fission of the Pt isotopes, obtained in the reaction ^{36}Ar + ^{142}Nd within the two-stage fusion-fission model

V. L. Litnevsky[*]
Omsk State Transport University, 644046 Omsk, Russia

F. A. Ivanyuk[†]
Institute for Nuclear Research, 03028 Kiev, Ukraine

G. I. Kosenko[‡]
Omsk Tank Automotive Engineering Institute, 644098 Omsk, Russia

S. Chiba[§]
Tokyo Institute of Technology, 152–8550 Tokyo, Japan

(Received 1 April 2019; published 24 May 2019)

The two-stage dynamical stochastic model developed earlier for the description of fusion-fission reactions is applied to the calculation of mass and energy distributions of fission fragments of platinum isotopes in the reaction $^{36}\mathrm{Ar} + {}^{142}\mathrm{Nd} \rightarrow {}^{178-x}\mathrm{Pt} + xn$. The first stage of this model is the calculation of the approaching of the projectile nucleus to the target nucleus. In the second stage, the evolution of the system formed after the touching of the projectile and target nuclei is considered. The evolution of the system in both stages is described by three-dimensional Langevin equations for the shape parameters of the system. The mutual orientation of the colliding ions and tunneling through the Coulomb barrier in the entrance channel are also taken into account. The potential energy of the system is calculated within the macroscopic-microscopic approach. The calculated mass-energy distributions of fission fragments are compared with the available experimental data. The impact of shell effects, rotation of the system, and neutron evaporation on the calculated results is discussed.

DOI: 10.1103/PhysRevC.99.054624

I. INTRODUCTION

The first theoretical description of nuclear fission discovered in 1939 [1,2] was given in the framework of the liquid drop model [3] in which it is assumed that the properties of the atomic nucleus are similar to those of a charged viscous incompressible liquid drop. It turned out that the liquid drop model predicts splitting of the fissioning nucleus into two fragments with the same masses, which was confirmed by experiments of highly excited nuclei. However, in the case of low excitation energies, such as the fission of ^{235}U by thermal neutrons, the masses of the fission fragments are not equal. The explanation of mass-asymmetric fission was given later by the influence of shell effects. The presence of a mass-asymmetric fission valley for transuranium elements was demonstrated by Pashkevich in Ref. [4]. In this paper, the dependence of the potential energy of nuclei on their deformation was constructed using the shell correction method of Strutinsky [5] and Brack *et al.* [6], and it was shown that the fission process is strongly affected by the deformation dependence of the potential energy of the system. Further progress in the description of the process of nuclear fission is associated with the use of statistical [7,8] and dynamical [9,10] models as well as their combinations [11]. These models describe the fission of a nucleus initially located in a potential well near the ground state (g.s.) (compound nucleus). Such an excited compound nucleus can be formed by the irradiating of atomic nuclei by light particles. A fully microscopic stochastic description of the fission process was developed in Ref. [12]. The first application of this approach to a realistic physical phenomenon (spontaneous fission of ^{258}Fm) is presented in recent publications [13,14].

The description of the fission process becomes much more complicated if the excited nucleus is formed in the result of a fusion reaction of two massive ions. In this case, one can not talk merely about the fission of the compound nucleus. From the moment of touching of the initial nuclei to the moment of formation of the compound nucleus passes quite a long time during which the system may undergo fission or may reduce its excitation energy by emitting a light particle or γ quanta and form the compound nucleus in the g.s. As a result, for the description of the mass distribution of fission fragments it is necessary to consider the whole evolution of the fusion-fission process starting from the approach of the initial nuclei to each other and ending with the formation of a compound nucleus or fission.

[*]vlad.lit@bk.ru
[†]ivanyuk@kinr.kiev.ua
[‡]kosenkophys@gmail.com
[§]chiba.satoshi@nr.titech.ac.jp

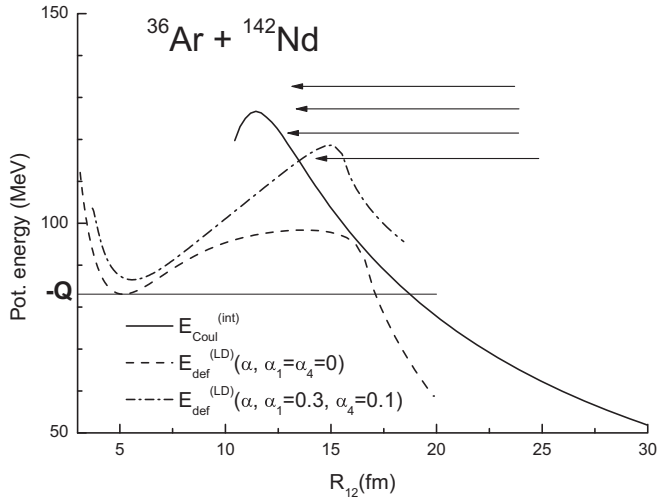

FIG. 1. The potential-energy $V^I_{\rm pot}$ (5) of colliding ions ^{36}Ar and ^{142}Nd in the entrance channel (solid curve) and the liquid drop deformation energy of ^{178}Pt for mass-symmetric ($\alpha_3 = \alpha_4 = 0$, dashed curve) and mass-asymmetric ($\alpha_3 = 0.3$, $\alpha_4 = 0.1$, dot-dashed curve) shapes as a function of the distance r between centers of mass. The horizontal line is the Q value of reaction $^{36}\mathrm{Ar} + {}^{142}\mathrm{Nd} \longrightarrow {}^{178}\mathrm{Pt}$.

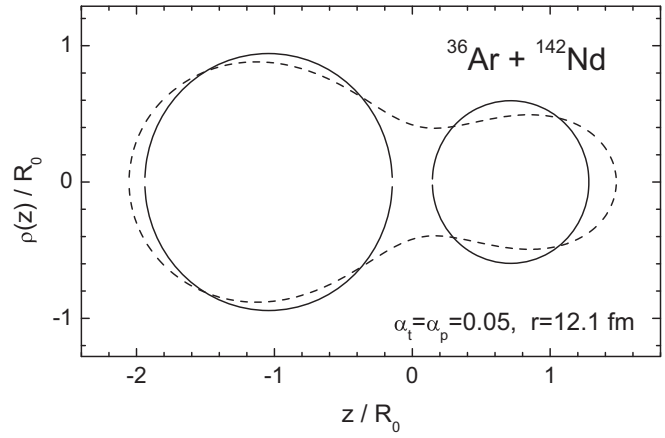

FIG. 2. An example of the touching configuration of ^{36}Ar and ^{142}Nd ($r = 12.1$ fm, $\alpha_t = \alpha_p = 0.05$, solid curve) and the fit by three-dimensional $(\alpha, \alpha_1, \alpha_4)$ Cassini ovaloids (dashed curve).

For this purpose, in Refs. [15–17], the so-called two-stage dynamic stochastic model for the description of a fusion-fission reaction with heavy ions was developed. In this model, in the first stage of calculations, the approaching of the projectile nucleus to the target nucleus up to their touching point is considered. In the second stage, the evolution of the compact system, formed after merging of colliding nuclei, is studied.

In the present paper, we apply the two-stage model [15–17] for the description of the kinetic energy (KE) and mass distributions of the fission fragments obtained in a recent publication [18] for the reaction $^{36}\mathrm{Ar} + {}^{142}\mathrm{Nd} \rightarrow {}^{178-x}\mathrm{Pt} + xn$ at beam energies $E_{\rm lab} = 153.9$, 168.8 and 178.8 MeV. This paper contains experimental data on the energy and mass distributions of fission fragments, average energy taken away by the prefission neutrons, the average induced angular momentum, and the rotational energy. Comparison of such data with calculated results would be a good test for the theoretical models.

II. THE TWO-STAGE APPROACH

As was mentioned above, in the first stage of the calculations, we consider the approaching of the projectile nucleus to the target nucleus up to their touching point. In the second stage, we study the evolution of the compact system, formed after the merging of colliding nuclei. The schematic comparison of the potential energy in fusion and fission channels is shown in Fig. 1. The final point of the second stage calculations could be the splitting of the system back into two fragments or the formation of the evaporation residue $^{178-x}$Pt, where x is a number of neutrons, evaporated by the compound system in order to reduce its excitation energy. Of course, the outcome depends on the reaction energy.

The evolution of both separated ions and compact system is described by Langevin equations for the collective parameters that fix the shape of the system. For the approaching process, the collective parameters are the parameters α_p and α_t of quadrupole deformation for both ions and the distance r between their centers of mass. In the approaching stage, we also take into account the orientation of the target nucleus—the angle θ_t between the symmetry axis of the deformed ions in the g.s. target nucleus and the line connecting the centers of mass of colliding nuclei.

The shape of the compact system is described by the parameters α, α_1, and α_4 of Cassini parametrization [4] that specify the total elongation, the mass asymmetry, and the neck radius of the system.

At the end of the first stage calculations (at the touching point), we fix the center-of-mass (c.m.) distance and the potential and internal (dissipated) energies of the system. At the initial point of the second stage calculations, we use these data to define the shape of the system, formed after the collision of the initial nuclei. To do it, we use three conditions. First, we fix α_4 and define α and α_1 from the requirement that the c.m. distance r and the mass asymmetry of separated ions and the compact system are the same. Then, we vary α_4, and among all possible shapes, which satisfy that requirement, choose the one, that corresponds to the lowest potential-energy $E_{\rm def}(\alpha, \alpha_1, \alpha_4)$ of the compact shape. An example of the relation between the shapes of separated ions and the compact system is shown in Fig. 2.

At both stages of the calculation, the time evolution of the collective degrees of freedom $\mathbf{q} \equiv \{\alpha, \alpha_n\}$ and corresponding momenta $\mathbf{p/m} \equiv \{\dot\alpha, \dot\alpha_n\}$ is described in terms of the Langevin equations [19,20], namely,

$$\dot q_\beta = \mu_{\beta\nu} p_\nu,$$
$$\dot p_\beta = -\frac{1}{2} p_\nu p_\eta \frac{\partial \mu_{\nu\eta}}{\partial q_\beta} + K_\beta - \gamma_{\beta\nu}\mu_{\nu\eta} p_\eta + \theta_{\beta\nu}\xi_\nu. \quad (1)$$

Here, q_β's are the deformation parameters, and a convention of summation over repeated indices ν, η is used. The quantity $\gamma_{\beta\nu}$ is the tensor of friction coefficients, and $\mu_{\beta\nu}$ is the tensor inverse to the mass tensor $m_{\beta\nu}$, K_β is a component of the conservative force $\vec{K} = -\nabla F$, where $F = V_{\rm pot} - aT^2$ is the free energy of the system, $V_{\rm pot}$ is the potential (deformation) energy, a is the level-density parameter [8], and the temperature T of the system is related to the internal (dissipated) energy by the Fermi-gas formula $T = \sqrt{E_{\rm dis}/a}$.

The friction force leads to the dissipation of collective motion energy into internal energy. The fluctuations in the system are described by the random force $\theta_{\beta\nu}\xi_\nu$. Here, ξ_ν is a random number with the following properties:

$$\langle \xi_\nu \rangle = 0,$$
$$\langle \xi_\beta(t_1)\xi_\nu(t_2)\rangle = 2\,\delta_{\beta\nu}\delta(t_1 - t_2). \quad (2)$$

The magnitude of the random force $\theta_{\beta\nu}$ is expressed in terms of diffusion tensor $D_{\beta\nu} = \theta_{\beta\eta}\theta_{\eta\nu}$, which is related to the friction tensor $\gamma_{\beta\nu}$ via the modified Einstein relation $D_{\beta\nu} = T^*\gamma_{\beta\nu}$, where T^* is the effective temperature [21].

The internal energy of the system could be calculated from the energy conservation condition,

$$E_{\rm c.m.} = V_{\rm pot} + E_{\rm kin} + E_{\rm dis}, \quad (3)$$

here $E_{\rm c.m.} = E_{\rm lab}A_{\rm Nd}/(A_{\rm Nd} + A_{\rm Ar})$ is the reaction energy, calculated in the c.m. system, and $E_{\rm kin}$ is the kinetic energy of the collective motion.

Some terms of Eq. (1) should be determined twice, one for the first, and one for the second stage of the calculations. Such terms we will denote by the upper indices (I) and (II), respectively.

The deformation energies $E_{\rm def}^{(t)}$ and $E_{\rm def}^{(p)}$ of colliding ions and $E_{\rm def}$ of the combined system are calculated within the macroscopic-microscopic shell-correction approach proposed by Pashkevich [4], Strutinsky *et al.* [5], and Brack *et al.* [6]. The interaction potential between the colliding ions consists of Coulomb part $V_{\rm Coul}$ [22] and nuclear Gross-Kalinowski potential $V_{\rm GK}$ [23], modified in order to describe the interaction of deformed ions [20]. The rotation of the system is taken into account in both stages of the calculations,

$$E_{\rm rot}^{I} = \frac{\hbar^2 L(L+1)}{2(Mr^2 + J_t + J_p)}, \qquad E_{\rm rot}^{II} = \frac{\hbar^2 L(L+1)}{2J}, \quad (4)$$

where $M = M_t M_p/(M_t + M_p)$ is the reduced mass of the target and the projectiles J_t, J_p, and J are the rigid body moments of inertia of the target, projectile nucleus, and of the combined system, respectively, and L is an angular momentum of the whole system.

Finally, the potential energy of the system is as follows:

$$V_{\rm pot}^{I} = V_{\rm Coul} + V_{\rm GK} + E_{\rm def}^{(t)} + E_{\rm def}^{(p)} + E_{\rm rot}^{I}, \quad (5)$$

$$V_{\rm pot}^{II} = E_{\rm def} + E_{\rm rot}^{II}. \quad (6)$$

Besides the deformation energy, the dynamical properties of each nucleus are characterized by the friction $\gamma_{\beta\nu}$ and inertia $m_{\beta\nu}$ tensors, that were calculated within the linear-response approach and local harmonic approximation [24,25]. In this approach, many quantum effects, such as shell and pairing effects, the dependence of the collisional width of single-particle states on the excitation energy, are taken into account. The precise expressions for the components of the friction $\gamma_{\beta\nu}$ and inertia $m_{\beta\nu}$ tensors can be found in Ref. [26]. Tensors $\gamma_{\beta\nu}$ and $m_{\beta\nu}$ [26] characterize completely the inertia and friction properties of the combined system and were used in our previous calculations within the three-dimensional Langevin approach with Cassini shape parametrization and the two-center shell-model shape parametrization [27].

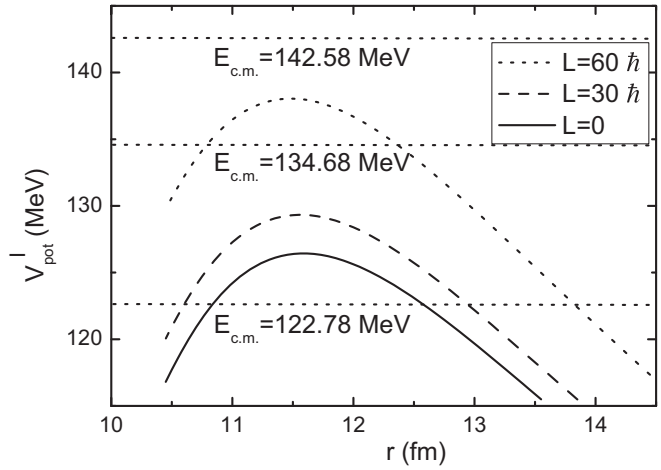

FIG. 3. The potential energy of the system as a function of distance r between target and projectile. The orientation of target $\theta_t = 0$, deformation parameters α_t and α_p correspond to the ground-state shapes of the target and projectile ions.

For the first stage of the calculation, besides the internal processes in ions, one should account also for their relative motion. The inertial tensor $m_{\beta\nu}^{I}$ in this case has only diagonal components: $m_{\rm rr}^{I} = M$ (reduced mass), $m_{\alpha_t\alpha_t}^{I} = m_{\alpha\alpha}^{\rm t}$, $m_{\alpha_p\alpha_p}^{I} = m_{\alpha\alpha}^{\rm p}$, and $m_{\theta_t\theta_t}^{I} = J_{\rm t}$. The friction tensor for the first stage of the process was defined as the sum of the friction tensor for the relative motion, obtained in the surface-friction model [28], such as was performed in Ref. [29], and the diagonal friction tensor for colliding ions, which has only two nonzero components ($\gamma_{\alpha_t\alpha_t}^{I} = \gamma_{\alpha\alpha}^{\rm t}$; $\gamma_{\alpha_p\alpha_p}^{I} = \gamma_{\alpha\alpha}^{\rm p}$).

III. THE RESULTS OF FIRST STAGE CALCULATIONS

In the present paper, the first stage calculations were stopped as soon as the system overcame the potential barrier. The position of the barrier depends on deformations and orientation of the colliding ions. It depends also slightly on the angular momentum of the system (see Fig. 3).

As one can see, some experimental data in Ref. [18] are obtained for the subbarrier energies. In order to describe such reactions, we took into account the quantum tunneling through the potential barrier. The penetrability of the barrier was defined in the Wentzel-Kramers-Brillouin approximation [30] as

$$T_L(E) = \left[1 + \exp\left(\frac{2}{\hbar}\int_{r_2}^{r_1}\sqrt{2m(V^{\rm fus} - E)}dr\right)\right]^{-1}, \quad (7)$$

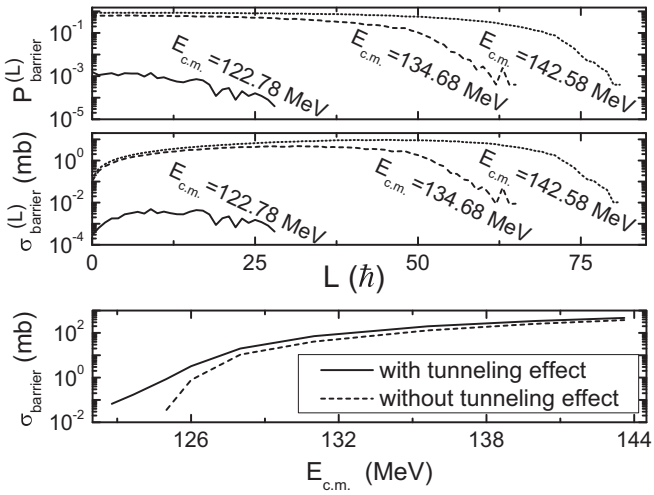

FIG. 4. The dependence of the probability (top) and the partial cross section (middle) of the penetration through the potential barrier, calculated with an account of the tunneling effect, on the angular momentum of the system. Bottom: the dependence of the cross section of the penetration through the potential barrier on the reaction energy.

where the integration is carried out between the turning points r_1 and r_2 in the subbarrier region and E is the incident energy, equal to the potential energy of the system at the turning points. As one can see from Fig. 4 (bottom), the account of quantum tunneling increases substantially the probability of penetration through the barrier in the subbarrier region.

The angular momentum is a free parameter of our model. So, the first stage calculations are carried out for a set of L. One can see from Fig. 3 that the height of the potential barrier increases with the angular momentum of the system. The probability to overcome the barrier will decrease in this case, see Fig. 4. Knowing the probability of an event, we can calculate its partial, Fig. 4 (middle) and total, Fig. 4 (bottom), cross sections, respectively,

$$\sigma^L_{\rm barrier}(L, E_{\rm c.m.}) = \pi\lambda^2(2L+1)P_{\rm barrier}(L, E_{\rm c.m.}), \quad (8)$$

$$\sigma_{\rm barrier}(E_{\rm c.m.}) = \sum_L \sigma^L_{\rm barrier}(L, E_{\rm c.m.}). \quad (9)$$

The main goal of the first stage calculations is to obtain the potential-energy $V^I_{\rm pot}$ of the system and its internal (dissipated) energy $E_{\rm dis}$ at the touching point.

Having at our disposal the distributions given in Fig. 4 (middle) and Figs. 5(b)–5(d), we can specify (by the hit-and-miss method) the initial values of angular momentum, internal and potential energies of the system for the beginning of the second stage of the calculations. The way to choose the initial shape parameters of the combined system was discussed in the previous section, see Fig. 2 and the text around it. So, the initial values for the second stage calculations are defined by the final data from the first stage,

$$E^{II}_{\rm kin,in}(L) = E^I_{\rm kin}(L),$$
$$E^{II}_{\rm dis,in}(L) = E^I_{\rm dis}(L) + V^I_{\rm pot} - V^{II}_{\rm pot}. \quad (10)$$

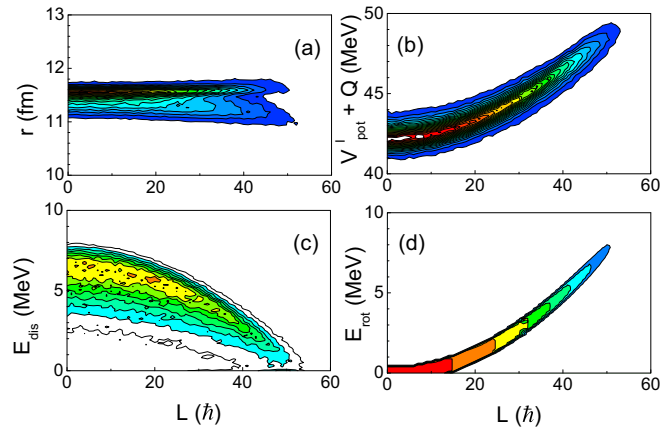

FIG. 5. The distributions of (a) c.m. distance, (b) potential, (c) dissipated, and (d) rotational energies of the system as functions of angular momentum L at the touching point for $E^* = 50.5$ MeV.

In order to bring $V^{II}_{\rm pot}$ and $V^I_{\rm pot}$ to the same scale, the so-called Q value of the reaction should be added to $V^{II}_{\rm pot}$,

$$V^{II}_{\rm pot,in} \longrightarrow V^{II}_{\rm pot,in} + Q, \quad (11)$$

where $Q < 0$ is defined in terms of g.s. energies of the target, projectile, and combined system $Q \equiv E^{(t+p)}_{\rm g.s.} - E^{(t)}_{\rm g.s.} - E^{(p)}_{\rm g.s.}$. One can define also the excitation energy E^* of reaction by the relation,

$$E^* = E_{\rm c.m.} + Q. \quad (12)$$

The distribution in Fig. 5(d) is the distribution of rotational energy at the touching point. The width of this distribution is very small. The contribution to this width comes from the uncertainty of c.m. distance r [which is also small, see Fig. 5(a)] that appears in the moment of inertia in Eq. (4).

Each point in Fig. 5(d) is the contribution of trajectory "i" that reached the touching point. By summing over all trajectories, one can define the average angular momentum $\langle L\rangle$ and the average rotational energy $\langle E_{\rm rot}\rangle$ of the system at the touching point,

$$\langle L\rangle = \sum_i L_i \Big/ \sum_i 1, \quad \langle E_{\rm rot}\rangle = \sum_i E^i_{\rm rot} \Big/ \sum_i 1. \quad (13)$$

The summation over trajectories based on distribution of Fig. 5(d) leads to the values of $\langle L\rangle \approx 20.5\hbar$ and $\langle E_{\rm rot}\rangle \approx 1.89$ MeV. In the same way, we can calculate the average value of dissipated energy $\langle E_{\rm dis}\rangle \approx 4.40$ MeV. As we can see, the sum of rotational and dissipated energies at the touching point is not so large compared with the excitation energy $E^* = 50.5$ MeV.

IV. THE EVOLUTION OF THE COMPACT SYSTEM

The potential-energy surface (PES) of ^{178}Pt in coordinates r-mass asymmetry $(A_L - A_R)/(A_L + A_R)$ is shown in Fig. 6. The star in this figure marks the position of the initial point corresponding to the shape shown in Fig. 2.

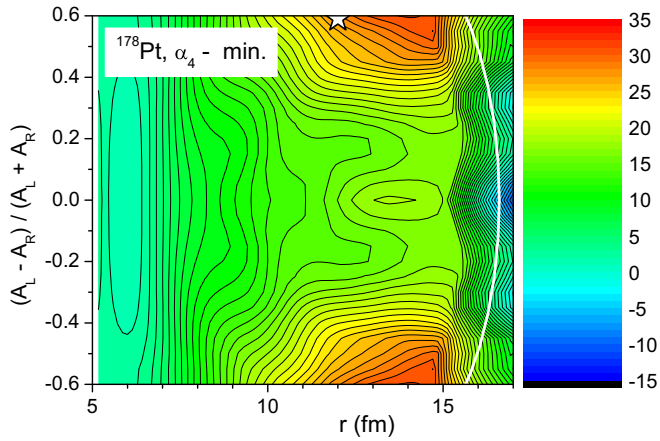

FIG. 6. The minimized, with respect to α_4, deformation energy of ^{178}Pt at $T = 0$. The white line marks the position of the zero neck for $\alpha_4 = 0$.

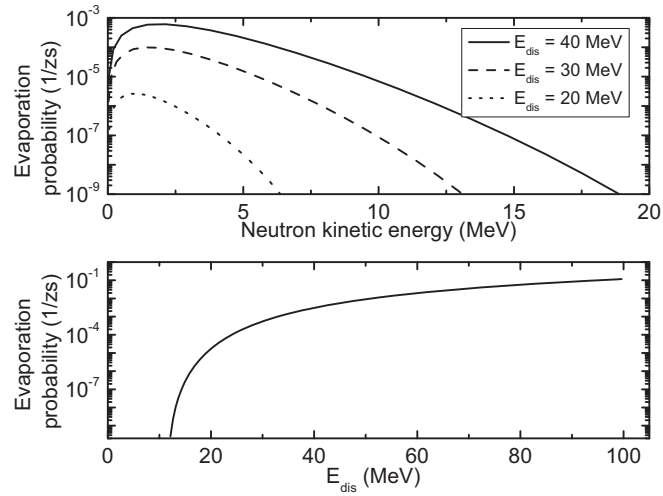

FIG. 7. The neutron evaporation probability (per zeptosecond) as a function of the neutron KE (top) and nuclear internal energy $E_{\rm dis}$ (bottom).

Starting from the touching point, the system would move in the direction of the g.s. under the action of the random force, form the compound nucleus, and then undergo fission. The evolution of the compound nucleus could last long enough to evaporate γ's or light particles, so we should take into account this deexcitation process. The evaporation of particles and γ quanta by the excited compact system is described in our approach within the statistical model [8]. On each integration step, the partial width of the corresponding decay channel [8] is calculated, then by the hit-and-miss method, we decide whether some particle was emitted and which kind of particle was emitted. If some particle was emitted, the binding energy of this particle was subtracted from the excitation energy of the system. Also, the particle can carry away some energy (its KE).

The main evaporation channel is the evaporation of neutrons. The probability of the neutron evaporation and its KE depends on the dissipated energy of the system as shown in Fig. 7. One can see that the system with dissipated energy $E_{\rm dis} = 40$ MeV, for example, should live, on average, 400 zs before the first neutron is evaporated. After evaporation, it loses about 10 MeV as a neutron kinetic and binding energy, so, to evaporate the second neutron, it needs about 1500 zs, and so on. Of course, during this evolution time there is a competition between neutron evaporation and fission. The fission of the nucleus can occur before it evaporates any neutron (dashed curve), or it could evaporate one (short dashed curve), two (dotted curve), or more neutrons before fission (see Fig. 8). The maximal number of the evaporated neutrons depends on the initial excitation energy of the system E^*, see Eq. (12).

After evaporation of several neutrons, the system's internal energy decreases, and the role of the nuclear shell structure becomes more and more significant. In Fig. 9, one can see the evolution of fragment mass distribution due to the deexcitation process (for the initial excitation energies $E^* = 39.6$ and $E^* = 50.5$ MeV). The mass distribution is symmetric if the system undergoes fission before it evaporates any neutron. Then, after the first neutron evaporation, the system slightly cools down, and the influence of the shell effects will be noticeable. And, finally, after the second neutron evaporation, the distribution becomes strongly mass asymmetric.

The total mass distribution obtained by superimposing of distributions shown in Fig. 9 is compared in Fig. 10 with the experimental data [18]. One can see that the calculated mass distributions for all three values of excitation energy E^* are very close to the experimental data.

V. THE TOTAL KINETIC ENERGY

The mass-energy distribution of fission events is shown in the left part of Fig. 11. In these calculations, for each trajectory that reached the scission point $\{q_i\}$, we define the total kinetic-energy TKE$_i$ as the sum of the Coulomb interaction

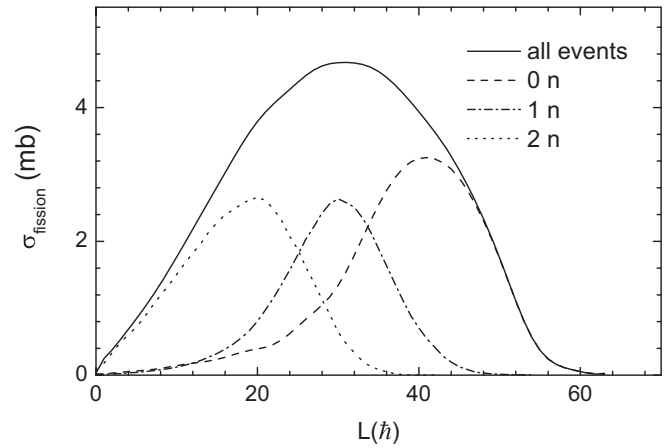

FIG. 8. The partial cross sections of the fission process in the case of zero (dashed curve), one (dashed-dotted curve), and two (dotted curve) neutrons emitted by the compound nucleus before fission as a function of angular momentum of the system. The solid curve is the partial cross sections of all fission events.

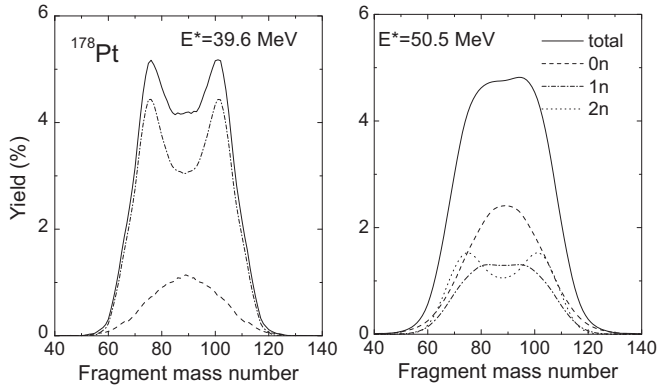

FIG. 9. The contributions to the total fission cross section of ^{278}Pt (solid curve) at $E^* = 39.6$ and 50.5 MeV of the fission events without neutron evaporation (dashed curve), with evaporation of one neutron (dashed-dotted curve), and with evaporation of two (dotted) neutrons.

of spherical fragments at the scission point and prescission kinetic-energy $\mathrm{KE}^{(\mathrm{pre})}$,

$$\mathrm{TKE}_i = E^{(\mathrm{int})}_{\mathrm{Coul}}(q_i) + KE^{(\mathrm{pre})}_i. \tag{14}$$

Here,

$$E^{(\mathrm{int})}_{\mathrm{Coul}}(q_i) \equiv Z_L Z_H e^2/r(q_i), \tag{15}$$

where eZ_L and eZ_H are the charges of light and heavy fragments. The prescission kinetic-energy $\mathrm{KE}^{(\mathrm{pre})}_i$ is the kinetic energy in the fission direction obtained from the solutions of Langevin equations at the scission point. It turned out in these calculations that the average value of $\mathrm{KE}^{(\mathrm{pre})}$ is very small, on the order of 1 to 2 MeV, and the main contribution to TKE comes from the Coulomb repulsion energy.

The TKE distribution of fission fragments is shown in the right part of Fig. 11. The shape of the distribution is very

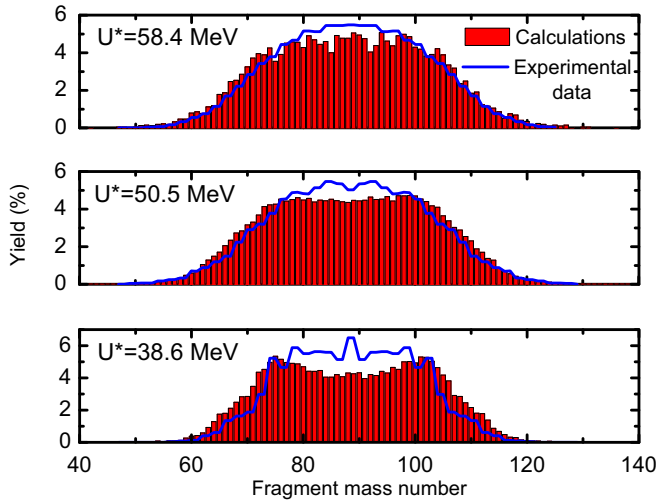

FIG. 10. The calculated fission fragment mass distributions in comparison with the experimental data [18].

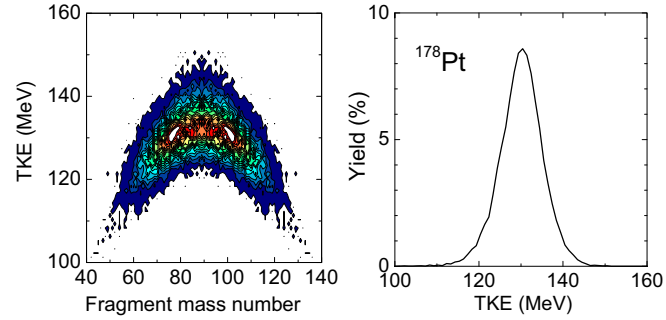

FIG. 11. Left: The mass-energy distribution of fission events for $E^* = 50.5$ MeV. Right: The normalized to 100% yield of fission fragments as function of the total kinetic energy.

close to a single Gaussian. We did not find the contributions to TKE distribution from the two fission modes as was argued in Ref. [18]. We see the two fission valleys on the potential-energy surface at large elongation, beyond the saddle point, see Fig. 12. Between saddle and scission, the mass-symmetric valley is even deeper compared with the mass-asymmetric valley. However, it follows from the calculations that the dynamical trajectories do not follow the bottom of the fission valley. The mass and energy distributions are formed mainly at the saddle. The trajectories spend a lot of time inside the saddle. Some of them reach the saddle and move very quickly towards the scission. The descent from saddle to scission in ^{178}At (and other light fissioning nuclei) is very short, see Fig. 12, and steep. The trajectories do not have much time to adjust themselves to the potential-energy landscape during saddle-to-scission motion. Note also that the mass asymmetry of the asymmetric valley beyond the saddle is much larger as

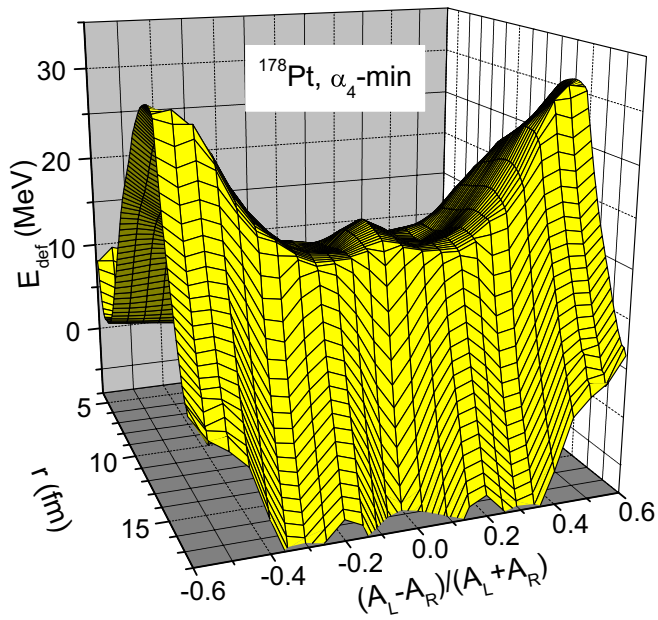

FIG. 12. The "backside" of the PES: the saddle-to-scission part of the deformation energy of ^{278}Pt minimized with respect to α_4 at $T = 0$.

(coinciding with experimental) the mass asymmetry of PES at the saddle.

The average value of the TKE is equal to 130.4 MeV, which is rather close to the position of the main peak $\mathrm{TKE}^{\mathrm{high}} = 133.4$ MeV in experimental results [18]. The width of TKE-distribution $\sigma_{\mathrm{TKE}} = 11$ MeV is, however, much smaller than experimental value, see Fig. 2(a) of Ref. [18].

We tried hard to increase σ_{TKE} and did not succeed. For the following reason: The contribution to the total kinetic energy comes from the fragments' prescission KE and the fragments' Coulomb repulsion energy immediately after scission, see Eqs. (14) and (15). Since the prescission KE is very small in the considered case, only a few MeV, the main part of the TKE is the Coulomb repulsion energy $E_{\mathrm{Coul}}^{(\mathrm{int})}$. In Eq. (15), $r(q_i)$ is an only variable quantity. In order to get the value of TKE = 70 MeV (that is the smallest experimental value of the TKE for symmetric splitting at $E^* = 50.5$ MeV), r should be close to 30 fm. Taking into account that the distance between centers of mass for the touching configuration of ^{36}Ar and ^{142}Nd is only $r \approx 10.4$ fm, it is not difficult to come to the conclusion that there is no way to produce a compact shape of ^{178}Pt with extremely large elongation $r \approx 30$ fm. Such a compact shape should break apart much earlier at smaller values of r. So, we do not see many chances to get the fission events with TKE = 70 MeV.

The difference between calculated and experimental values of σ_{TKE} might be attributed to the uncertainty of the scission point configuration formed in the reaction, the finite (in)accuracy of TKE measurements, and some limitations of the theoretical approach. In particular, the generalization of the three-dimensional Langevin approach to a four-dimensional approach would increase the variety of shapes at the scission point and, thus, could increase the width of TKE distribution.

VI. CONCLUSIONS

Within the developed earlier two-stage approach for the fusion-fission reactions, we have studied the reaction $^{36}\mathrm{Ar} + {}^{142}\mathrm{Nd} \rightarrow {}^{178-x}\mathrm{Pt} + xn$. The obtained results are compared with the available experimental data [18]. The calculated mass distributions of fission fragments for three energies $E_{\mathrm{c.m.}} = 122.78$, 134.68, and 142.58 MeV are in good agreement with the experimental results. The most probable mass division for the asymmetric component of fission fragments mass distribution (Fig. 10) is found to be about $A_{\mathrm{L}}/A_{\mathrm{H}} = 79/98$, which is rather close to the experimental data [18]. From our calculations, it follows that the competition between symmetric and asymmetric fission channels is caused by the enhancement of shell effects in the compound nucleus due to the process of its deexcitation by neutron emission.

The average value of the TKE is equal to 130.4 MeV, which is rather close to the position of the main peak $\mathrm{TKE}^{\mathrm{high}} = 133.4$ MeV in experimental results. The calculated shape of distribution is very close to a single Gaussian. We did not find the contributions to TKE distribution from two fission modes as was argued in Ref. [18].

From the results of the calculations, it follows that the dynamical trajectories do not follow the bottom of the fission valley and the mass distribution of fission fragments of ^{178}Pt is formed mainly at the saddle.

ACKNOWLEDGMENTS

This study includes the results of "Research and development of an innovative transmutation system of LLFP by fast reactors," entrusted to the Tokyo Institute of Technology by the Ministry of Education, Culture, Sports, Science and Technology of Japan (MEXT). The authors would like to thank Prof. A. N. Andreyev and Prof. I. Tsekhanovich for useful discussions.

[1] O. Hahn and F. Strassmann, Naturwissenshaften **27**, 11 (1939).
[2] L. Meitner and O. R. Frisch, Nature (London) **143**, 239 (1939).
[3] N. Bohr and J. A. Wheeler, Phys. Rev. **56**, 426 (1939).
[4] V. V. Pashkevich, Nucl. Phys. **A169**, 275 (1971).
[5] V. M. Strutinsky, Nucl. Phys. A **95**, 420 (1967); **122**, 1 (1968).
[6] M. Brack, J. Damgaard, A. S. Jensen, H. C. Pauli, V. M. Strutinsky, and C. Y. Wong, Rev. Mod. Phys. **44**, 320 (1972).
[7] P. Fong, *Statistical Theory of Nuclear Fission* (Gordon and Breach, New York, 1969).
[8] A. S. Iljinov, M. V. Mebel, N. Bianchi, E. De Sanctis, C. Guaraldo, V. Lucherini, V. Muccifora, E. Polli, A. R. Reolon and, P. Rossi, Nucl. Phys. **A543**, 517 (1992).
[9] G. D. Adeev and V. V. Pashkevich, Nucl. Phys. **A502**, 405 (1989).
[10] M. D. Usang, F. A. Ivanyuk, C. Ishizuka, and S. Chiba, Sci. Rep. **9**, 1525 (2019).
[11] N. D. Mavlitov, P. Fröbrich, and I. I. Gontchar, Z. Phys. A **342**, 195 (1992).
[12] S. Ayik, Phys. Lett. B **658**, 174 (2008).
[13] Y. Tanimura, D. Lacroix, and S. Ayik, Phys. Rev. Lett **118**, 152501 (2017).
[14] Y. Tanimura, D. Lacroix, and S. Ayik, Phys. Rev. Lett. **121**, 059902(E) (2018).
[15] G. I. Kosenko, F. A. Ivanyuk, and V. V. Pashkevich, Phys. At. Nucl. **65**, 1588 (2002).
[16] V. L. Litnevsky, V. V. Pashkevich, G. I. Kosenko, and F. A. Ivanyuk, Phys. Rev. C **89**, 034626 (2014).
[17] V. L. Litnevsky, G. I. Kosenko, F. A. Ivanyuk, and V. V. Pashkevich, Phys. At. Nucl. **77**, 167 (2014).
[18] I. Tsekhanovich, A. N. Andreyev, K. Nishio *et al.*, Phys. Lett. B **790**, 583 (2019).
[19] Y. Abe, S. Ayik, P.-G. Reinhard, and E. Suraud, Phys. Rep. **275**, 49 (1996).
[20] J. Marten and P. Fröbrich, Nucl. Phys. **A545**, 854 (1992).
[21] H. Hofmann and D. Kiderlen, Int. J. Mod. Phys. E **07**, 243 (1998).
[22] R. S. Kurmanov, G. I. Kosenko, and G. D. Adeev, Phys. At. Nucl. **63**, 1885 (2000).
[23] D. H. E. Gross and H. Kalinovski, Phys. Rep. **45**, 175 (1978).
[24] H. Hofmann, Phys. Rep. **284**, 137 (1997).

[25] H. Hofmann, *The Physics of Warm Nuclei With Analogies to Mesoscopic Systems* (Oxford University Press, New York, 2008).

[26] F. A. Ivanyuk, in *Proceedings of International Conference on Nuclear Physics "Nuclear Shells-50"*, Dubna, Russia, 21–24 April 1999 (World Scientific, Singapore, 2000), p. 456.

[27] M. D. Usang, F. A. Ivanyuk, C. Ishizuka, and S. Chiba, Phys. Rev. C **94**, 044602 (2016).

[28] P. Fröbrich, Phys. Rep. **116**, 337 (1984).

[29] V. L. Litnevsky, G. I. Kosenko, F. A. Ivanyuk, and V. V. Pashkevich, Phys. At. Nucl. **75**, 1500 (2012).

[30] T. I. Nevzorova and G. I. Kosenko, Phys. At. Nucl. **71**, 1373 (2008).